CHAPTER FIFTEEN

An Optical Apparatus for Rotation and Trapping

Braulio Gutiérrez-Medina,[*,1,2] Johan O. L. Andreasson,[†,1] William J. Greenleaf,[‡,3] Arthur LaPorta,[§] *and* Steven M. Block[*,‡]

Contents

1. Introduction 378
2. Optical Trapping and Rotation of Microparticles 379
   2.1. The principles of optical manipulation 379
   2.2. Sources of particle anisotropy 382
3. The Instrument 385
   3.1. Overview 385
   3.2. The microscope 387
   3.3. Signal detection and processing 389
4. Fabrication of Anisotropic Particles 390
   4.1. Particles with shape asymmetry 390
   4.2. Particles with optical asymmetry 391
5. Instrument Calibration 395
   5.1. Standard optical tweezers calibration methods 395
   5.2. Force calibration 396
   5.3. Torque calibration 398
   5.4. Implementation of an optical torque clamp 398
6. Simultaneous Application of Force and Torque Using Optical Tweezers 400
   6.1. Twisting single DNA molecules under tension 400
7. Conclusions 402
Acknowledgments 402
References 403

[*] Department of Biology, Stanford University, Stanford, California, USA
[†] Department of Physics, Stanford University, Stanford, California, USA
[‡] Department of Applied Physics, Stanford University, Stanford, California, USA
[§] Department of Physics, Biophysics Program, Institute for Physical Science and Technology, University of Maryland, College Park, Maryland, USA
[1] These authors contributed equally to this work
[2] Present address: Instituto Potosino de Investigación Científica y Tecnológica, San Luis Potosí, Mexico
[3] Present address: Department of Chemistry and Chemical Biology, Harvard University, Cambridge, Massachusetts, USA

Methods in Enzymology, Volume 475
ISSN 0076-6879, DOI: 10.1016/S0076-6879(10)75015-1

Abstract

We present details of the design, construction, and testing of a single-beam optical tweezers apparatus capable of measuring and exerting torque, as well as force, on microfabricated, optically anisotropic particles (an "optical torque wrench"). The control of angular orientation is achieved by rotating the linear polarization of a trapping laser with an electro-optic modulator (EOM), which affords improved performance over previous designs. The torque imparted to the trapped particle is assessed by measuring the difference between left- and right-circular components of the transmitted light, and constant torque is maintained by feeding this difference signal back into a custom-designed electronic servo loop. The limited angular range of the EOM ($\pm 180^{\circ}$) is extended by rapidly reversing the polarization once a threshold angle is reached, enabling the torque clamp to function over unlimited, continuous rotations at high bandwidth. In addition, we developed particles suitable for rotation in this apparatus using microfabrication techniques. Altogether, the system allows for the simultaneous application of forces ($\sim$0.1–100 pN) and torques ($\sim$1–10,000 pN nm) in the study of biomolecules. As a proof of principle, we demonstrate how our instrument can be used to study the supercoiling of single DNA molecules.

1. Introduction

Optical tweezers have proved to be an extremely powerful tool in the investigation of biophysical processes, particularly the activity of motor proteins and other processive enzymes, whose biological activity involves converting chemical energy into mechanical work. The ability to measure displacements with subnanometer resolution and to apply piconewton-level forces in a controlled manner makes optical trapping ideal for studying the motion of biological macromolecules (Abbondanzieri *et al.*, 2005; Neuman and Block, 2004; Svoboda and Block, 1994). Through the use of active servo loops or passive optical configurations that can clamp the force, position, loading rate, or other physical quantities, precisely defined perturbations can be applied to identify the kinetic processes that underlie enzyme mechanisms.

Force and displacement, however, represent just one aspect of the physical picture. A host of important biomolecular complexes, including the F_1-ATPase (Noji *et al.*, 1997) and the bacterial flagellar motor (Berg, 2003), generate torque and rotation—rather than force and displacement—as the mechanical output. Moreover, owing to the helical structure of DNA, many processive nucleic-acid-based enzymes undergo rotation and generate torsional strain as a consequence of their translocation. Torsional strain in DNA and chromatin is regulated, directly and indirectly, by a

variety of proteins such as topoisomerases, helicases, gyrases, histones, and chromatin remodeling factors (Dong and Berger, 2008), and it is well established that such strain is a major factor in gene expression (Kar *et al.*, 2006). Finally, mechanoenzymes that translocate along linear polymers, such as myosin or kinesin, may also generate (or respond to) torque (Hua *et al.*, 2002). Practical benefit can therefore be gained by generalizing single-molecule methods to include the precise detection of rotation and the application of torque. Currently, the well-established technique of magnetic tweezers permits controlled rotation of magnetic microparticles by adjusting the orientation of an external magnetic field, enabling a variety of single-molecule manipulations. Magnetic tweezers are comparatively simple in their design and operation, and take advantage of the biologically noninvasive character of the magnetic field, typically producing constant forces over distances of several microns. However, conventional magnetic tweezers have certain practical limitations. There is no direct way to measure the torque imparted to the trapped particle, nor to conveniently record its angular displacement with respect to the applied field. Also, most magnetic tweezers determine displacement using frame-by-frame video processing of particle images, and are therefore limited by video acquisition rates, whereas laser-based optical trapping systems tend to use dedicated photosensors (quadrant photodiodes or position-sensitive detectors (PSDs)) with bandwidths exceeding several kilohertz. Finally, the magnitudes and directions of the fields produced by permanent or electromagnets cannot be changed very quickly, making it harder to adjust external control variables, such as the torque and force, as rapidly as one might like.

In the following sections, we describe the latest generation of an optical torque wrench (OTW), based on an improved design. Like conventional optical tweezers, the instrument has the ability to manipulate micron-sized particles, and to monitor both force and displacement. Additionally, it has the capacity to produce rotation, and to measure angle and applied torque with excellent precision ($\sim$1 pN nm of torque) at high bandwidth ($\sim$10–100 kHz).

2. Optical Trapping and Rotation of Microparticles

2.1. The principles of optical manipulation

A single beam, gradient-force optical trap is based on the interaction of a micron-sized dielectric particle with a beam of light that is brought to a diffraction-limited focal spot. Under the influence of the electric field (**E**), the particle develops an electric polarization **P** whose magnitude depends on material properties of the particle (Fig. 15.1A). For isotropic materials,

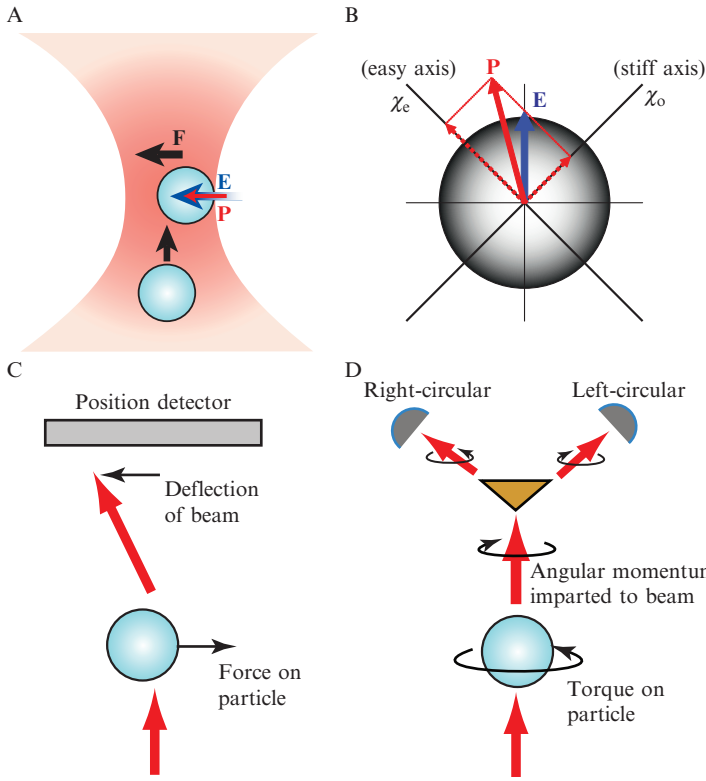

Figure 15.1 Principles of optical manipulation and signal detection. (A) The electric field (*E*, blue arrow) associated with a tightly focused laser beam induces a collinear electric polarization (**P**, red arrow) in an isotropic dielectric particle. As the particle moves away from the center of the laser focal volume, the induced dipole–electric field interaction produces a net restoring force (*F*, black arrows) toward the center, confining the particle in 3D. (B) For an optically anisotropic particle, different axes exhibit different polarizabilities. The induced polarization vector, therefore, is not collinear with the external electric field, and inclines toward the most polarizable (easy) axis. This effect gives rise to a net torque on the particle that tends to align the easy axis with the electric field. (C) Force can be detected by measuring trapping beam deflections (corresponding to changes in linear momentum) induced by an off-center, trapped particle, using a position-sensitive detector. (D) Analogously, the torque exerted by a linearly polarized beam on an anisotropic particle can be detected, based on the imbalance in the right- and left-circular polarization components in the beam after scattering by the particle, which can be measured independently.

$\mathbf{P} = \chi\mathbf{E}$, where χ is the polarizability of the material. The interaction of the induced polarization vector with the applied electric field leads to a net force proportional to $\chi\nabla E^2$, where ∇E^2 is the gradient of the electric field intensity (Ashkin, 2006; Ashkin *et al.*, 1986). In the presence of a highly

focused laser beam, a particle is therefore drawn toward the focal point, which constitutes the lowest energy state.

An electric dipole, $\mathbf{p}$, interacting with an external electric field can also generate a torque, in addition to force, whose magnitude is given by $\tau = |\mathbf{E} \times \mathbf{p}| = Ep \sin\theta$, where θ is the angle between $\mathbf{E}$ and $\mathbf{p}$. To produce nonzero torques, it follows that the net induced dipole moment must have a component perpendicular to the average external field. This condition can be satisfied using anisotropic particles, where either *form* or *material* birefringence (or both) lead to different polarizabilities along perpendicular axes. Form birefringence is a purely geometrical property, arising from the way that the shape of a small particle scatters light (e.g., an oblate ellipsoid), whereas material birefringence is an intrinsic optical property of the material from which the particle is produced (e.g., crystalline quartz). When an object is birefringent, the expression relating the induced dipole to the external field is replaced by the matrix equation $\mathbf{p} = \chi\mathbf{E}$, which reduces to the scalar relations $p_i = \chi_i E_i$ whenever the coordinate system coincides with the principal axes of a birefringent crystal, or with the symmetry axes of an anisotropic shape. Figure 15.1B illustrates an example where the external field makes an angle of 45° with respect to two principal axes. The induced dipole tends toward the easy optical axis, and the resulting torque acts to bring the most polarizable axis into alignment with the external field.

From Newton's laws, the amount of force and torque generated by an optical trap can be computed by considering linear and angular momentum, respectively, transferred from the laser beam to the trapped particle. A single photon carries energy $\varepsilon = hc/\lambda$, linear momentum $p = h/\lambda$, and the angular momentum associated with its spin is $L = \pm h/2\pi$ (for right- and left-circularly polarized light), where h is Planck's constant, c is the speed of light, and λ is the wavelength. The rate of change of linear momentum (equal to the force) is therefore given by $F = \mathrm{d}p/\mathrm{d}t = (1/c)\mathrm{d}\varepsilon/\mathrm{d}t$, or $F = \wp/c$, where $\wp = \mathrm{d}\varepsilon/\mathrm{d}t$ is the optical power. Similarly, the torque, τ, is equal to the rate of change of angular momentum, which leads to $\tau = (\lambda/2\pi c)\wp$. Assuming a laser with $\lambda = 1064$ nm and conversion efficiencies in the range of 1–10% (typical of optical traps, in practice), it follows that an optical trap might generate 0.03–0.3 pN of force and 6–60 pN nm of torque per milliwatt of incident optical power. When these values are compared with the forces needed to extend a coil of double-stranded DNA (dsDNA) (5 pN) (Smith *et al.*, 1992; Wang *et al.*, 1997) or to melt dsDNA (~100 pN) (Smith *et al.*, 1996), or with the torque necessary to unwind dsDNA (~10–100 pN nm) (Bryant *et al.*, 2003), it becomes clear that the linear and angular momentum carried by a laser beam is adequate to produce biologically relevant forces and torques at modest power.

Torque may also be applied to optically trapped particles by taking advantage of the "orbital" angular momentum of the light, which is associated with the geometry of the laser beam, rather than with the

individual photon spin. Practical implementations of this strategy include optical vortices and higher order Gaussian–Laguerre modes (He *et al.*, 1995; Volpe and Petrov, 2006), where the flow of energy (the Poynting vector) in the optical mode carries angular momentum about the beam axis. Orbital angular momentum can also be developed from a pair of ordinary laser beams that propagate along nonintersecting, nonparallel paths, or by using a spatially anisotropic trapping beam in conjunction with an asymmetrically shaped particle. In addition, torque is developed whenever microscopic *chiral* particles scatter light in such a way as to induce orbital angular momentum (Friese *et al.*, 2001). Although the changes in torque from an asymmetric trapping beam might, in principle, be measured (Simpson and Hanna, 2009), doing so would likely involve detecting subtle changes in the phase profile of the outgoing beam, requiring interferometric imaging of the outgoing trap beam and sophisticated real-time image analysis.

By contrast, the OTW represents a conceptually simpler arrangement, based on the ''spin'' angular momentum of light, which is associated with its polarization. The OTW scheme provides a straightforward way to apply and detect torque (La Porta and Wang, 2004) by monitoring the net change in the polarization of an optical trapping beam as it interacts with a transparent, anisotropic (birefringent) particle. The OTW controls rotation of the specimen by turning the polarization of the incoming beam, and determines the torque by separating the right- and left-circular components of the outgoing beam and measuring their intensities using standard polarization components. It then becomes possible to use a single trapping laser beam for both linear and angular manipulation, and the detection of force (Fig. 15.1C) and torque (Fig. 15.1D). The OTW has the additional advantage that the angular and linear trapping effects are relatively independent, with little crosstalk between them.

2.2. Sources of particle anisotropy

Two types of birefringence are suitable for producing the optical anisotropy necessary for use with an OTW: *form birefringence* and *material birefringence*. In form birefringence, a tiny particle with differing dimensions along perpendicular axes is easier to polarize along the more extended direction, provided that the dimensions are comparable to, or smaller than, the wavelength of the scattered light. Such a small particle will exhibit birefringence even when the material comprising the particle itself is isotropic, resulting in indirect coupling between the particle shape and the polarization of the trap beam. For optical rotation purposes, oblate particle symmetry is desirable, so that the two extended axes lead to stable orientation within the trapping beam and simultaneous alignment of the net polarization vector with the trapping electric field (see Fig. 15.2A). This configuration allows the particle to rotate, as necessary, to present the attachment

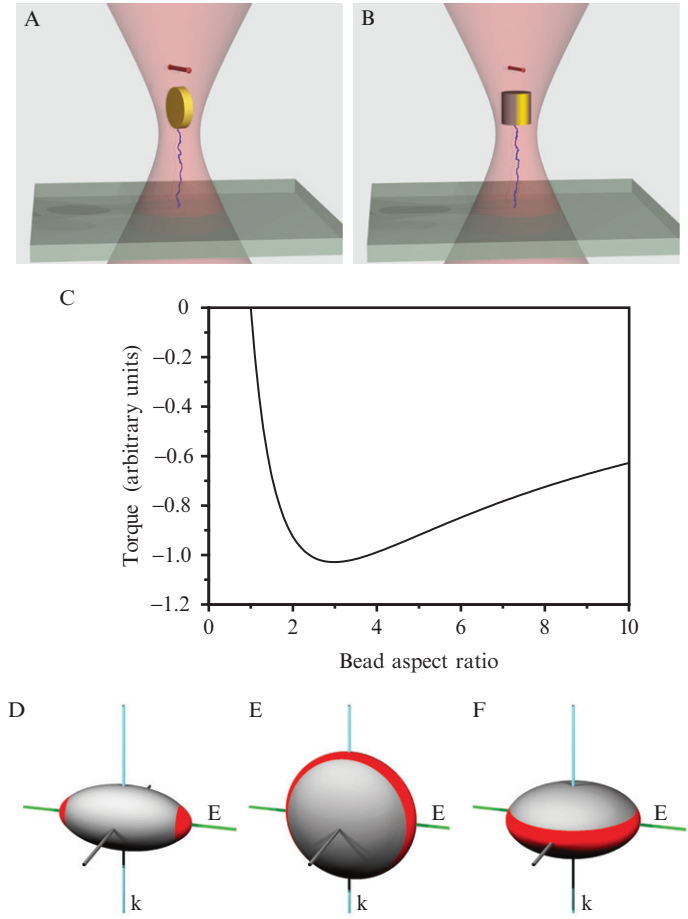

Figure 15.2 Particle anisotropy for optical trapping and rotation. (A) A small, oblate particle made of an optically isotropic material tends to align its long radii with the trapping beam axis (vertical) and the polarization direction (red arrow). (B) A birefringent cylinder tends to align its long axis with the trapping beam axis, allowing the extraordinary optical axis of the crystal to track the trap polarization direction. Possible materials for birefringent particles include quartz and calcite. (C) Theoretical estimate of the torque exerted on a subwavelength, oblate particle subjected to a uniform electric field, shown as a function of its aspect ratio (maximum to minimum radius). Bigger torques correspond to larger negative values; the greatest torque (curve minimum) occurs near an aspect ratio of 3. (D–F) The polarization ellipsoids for quartz (D), and calcite (E), (F) are shown, where red (gray) zones represent regions of maximum (minimum) electric susceptibility. Axes corresponding to red regions tend to align with the direction of the electric field vector **E** (green axis). For optical trapping and rotation, an ideal configuration is obtained when rotation is possible around the direction of the beam propagation vector, **k** (blue axis). This is the case for quartz (D). For calcite, the configuration shown in (E) can be used to exert torque (although alignment of the polarization ellipsoid with respect to the direction of **E** is not unique), whereas in the arrangement shown in (F) the particle exhibits no net birefringence on the plane perpendicular to **k** and no torque can be generated about the beam axial direction.

point of a biological molecule downward in response to upward tension (assuming an inverted microscope arrangement, with the laser beam introduced from below the objective) (Oroszi *et al.*, 2006).

An optimum aspect ratio for form birefringence that maximizes the torque for oblate particles can be derived ($\rho = r_{\max}/r_{\min}$), assuming that the particle is small compared to the wavelength of the trapping radiation. The torque exerted on an oblate ellipsoid in a uniform electric field is given by:

$$\tau = \frac{(\varepsilon - 1)^2(1 - 3\varepsilon)E^2 V \sin 2\alpha}{8\pi(\pi\varepsilon + 1 - n)([1 - n]\varepsilon + 1 + n)}, \tag{15.1}$$

where V is the volume of the particle, n is the depolarizing factor along the symmetry axis, ε is the dielectric constant, α is the angle between the electric field direction and the polar axis of the particle, and E is the electric field (Landau *et al.*, 1984). Assuming that volume is conserved, the torque asymptotically approaches a constant value as ρ goes to infinity, a limit that is not physically relevant, because the expression for torque is only valid when the major axis remains small compared to the size of the trapping beam. Instead, a meaningful optimization is obtained by varying the aspect ratio under the constraint that the major axis remains constant and on the order of the trap size, in which case the volume of the particle is proportional to ρ^{-1}. The torque, normalized to the incident electric field, E, is plotted in Fig. 15.2C: a maximum value is obtained with an aspect ratio of $\rho \approx 3$. The torque computed from Eq. (15.1) with this aspect ratio for an oblate ellipsoid made of silica is approximately 60% of the corresponding torque for a sphere of equivalent volume made from quartz, which is intrinsically birefringent.

The alternative to form birefringence is material birefringence. Birefringent materials have distinct principal axes exhibiting different polarizabilities. Some substances, such as quartz and calcite, have two (ordinary) axes that are equivalent, and one (extraordinary) axis that is different from the other two. For quartz, the extraordinary axis is the most easily polarized, and so the overall polarizability can be represented by a prolate ellipsoid. In the presence of an external electric field, quartz experiences a torque that tends to align the extraordinary axis with the electric field vector (Fig. 15.2D). For calcite, however, the extraordinary axis is the least polarizable, so the overall polarizability is represented by an oblate ellipsoid. In this case, the extraordinary axis is repelled from, and the two ordinary axes are drawn toward, the electric field vector (Figs. 15.2E and F). While it may be possible to exert torque on calcite particles using the configuration shown in Fig. 15.2E, quartz offers more optimized conditions for combined optical trapping (translation) and rotation. Inside an optical trap, quartz particles with prolate shapes can be stably trapped in a vertical orientation dictated by

their shape, then rotated about the optical axis due to the prolate polarizability ellipsoid.

Ideally, particles used in an OTW need to be strongly and stably trapped in all three dimensions, readily rotated, and functionally consistent with any planned biological experiments (e.g., functional attachment of the particles to macromolecules must be possible). One particularly important experimental geometry for single-molecule experiments is the surface-based assay, where the molecule of interest—for example, DNA—is tethered to the coverglass surface by one end and to the trapped particle by the other. In the OTW, force can then be applied upwards to stretch the tether while controlled rotation takes place around the vertical axis. For this purpose, the use of *cylindrical* quartz particles is particularly convenient (Fig. 15.2B). Cylinders whose length exceeds their diameter will naturally tend to align their long axis with the optical axis of the trap, and the extraordinary optical axis of the material can be chosen to lie parallel to the base and top of the cylinder, facilitating rotation in the horizontal plane (Deufel *et al.*, 2007). Micrometer-scale cylinders are also comparatively easy to fabricate, and their flat end-surfaces can be chemically derivatized to facilitate connections to biomolecules. In Section 4, we present detailed protocols to produce both oblate polystyrene ellipsoids and quartz cylinders.

3. The Instrument

3.1. Overview

The optical layout for the OTW is shown in Fig. 15.3, highlighting several differences compared with previous implementations (Deufel and Wang, 2006; La Porta and Wang, 2004; Oroszi *et al.*, 2006). A single laser beam is used both for optical trapping and rotation of microparticles, and for the simultaneous detection of force and torque. Rotation of the polarization in the sample plane is achieved by means of an electro-optic modulator (EOM), which replaces the pair of acousto-optic modulators (AOMs) used in a previous apparatus in an interferometer arrangement that shifted the relative phases of the vertical and horizontal polarization components of the input beam (La Porta and Wang, 2004).

Upon passage through the EOM, an incoming polarized light beam with electric field components (E_x, E_y) along the optical axes of the EOM crystal will experience a relative phase retardation (α) between E_x and E_y that is proportional to the applied voltage. The EOM thus behaves as a variable waveplate: it transforms an incoming linear polarization into elliptical polarization, where the degree of ellipticity is controlled by the voltage signal. After the EOM, the laser beam passes through an input $\lambda/4$-waveplate whose main optical axes are aligned at 45° with respect to those of the EOM, thereby

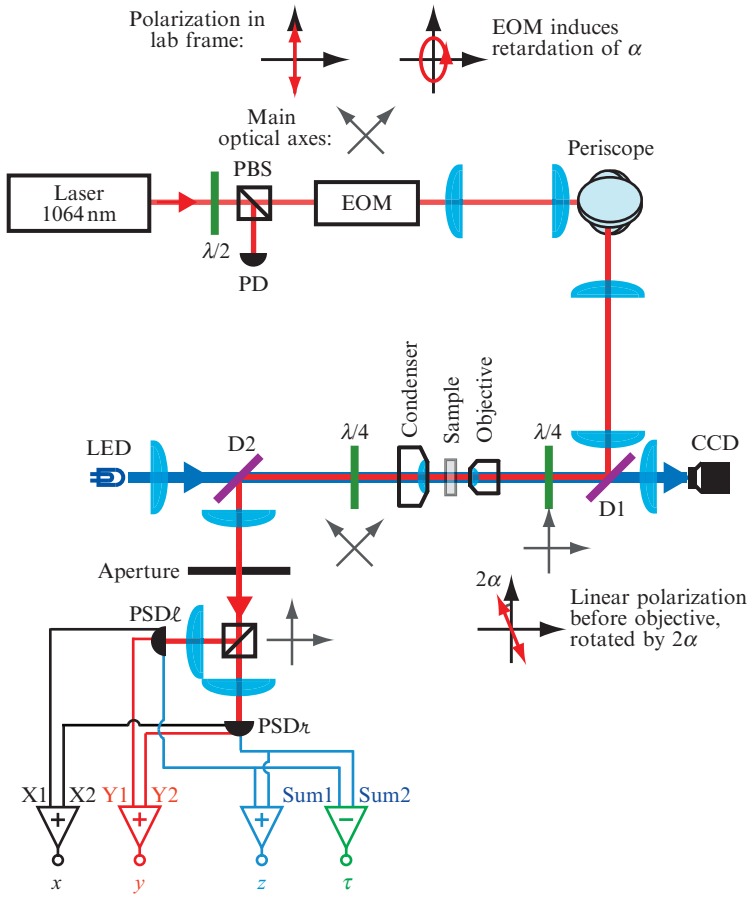

Figure 15.3 Optical schematic of the optical torque wrench. The trapping beam (thick red line) is produced by a near-infrared laser, and the output power is adjusted by a λ/2-waveplate and polarizing beam splitter (PBS). Rotation of linear polarization in the sample plane is achieved using an EOM and a λ/4-waveplate placed before the microscope objective. The optical axes for components relevant to torque generation and detection are shown (gray axes), along with the polarization state of the trapping beam as it travels along the optical path. To detect torque, a λ/4-waveplate is placed after the condenser to convert the polarization components from circular to linear; these are then separated by a PBS and measured using position-sensitive detectors (PSDℓ, PSDr). Each PSD produces *X*, *Y*, and Sum(*Z*) voltages, which are combined to yield *x*, *y*, *z*, and torque (τ) signals. D1, D2: dichroic mirrors; PD: photodiode; LED: blue light-emitting diode illuminator; CCD: charge-coupled device video camera.

restoring linear polarization, but now rotated by an angle $\theta = 2\alpha$ with respect to its initial orientation. One constraint of the EOM is that its dynamic range is limited, typically corresponding to $\alpha = \pm 90°$ (max). However, this limitation can be circumvented by implementing additional control electronics

(see Section 5.4). The use of an EOM offers several distinct advantages over a dual-AOM interferometer: (1) a symmetric beam profile is preserved throughout, which improves optical trap performance and calibration; (2) the polarization is no longer subject to significant long-term drift, as observed in the AOM-based system; and (3) the beam polarization angle is directly proportional to the EOM drive voltage, so there is no longer a need for additional input-angle detection optics. The new design is also considerably simpler to construct and align, involving fewer optical components.

3.2. The microscope

We now describe the instrument in further detail. The trapping beam is produced by a stable, diode-pumped solid-state Nd:YVO_4 laser (BL-106C, $\lambda = 1064$ nm, CW, Spectra Physics), operated near its peak power of 5 W to produce a beam with a clean TEM_{00} mode, with typical intensity fluctuations of $<0.2\%$. The optical power used for trapping is computer-controlled by means of a $\lambda/2$-waveplate mounted on a motorized rotary stage (PRM1-Z7E, Thorlabs) followed by a polarizing beam splitter (PBS). An alternative for controlling the power is an AOM; however, we found that the profile of the diffracted beam produced by an AOM was somewhat distorted, leading to an angular asymmetry in the trap that degraded the performance of the instrument. While a motorized stage is comparatively slow, rapid control of the intensity is nonessential, because trapping experiments are typically performed at constant power in the sample plane. After the PBS, the resulting beam has linear polarization of high purity ($>99.5\%$) and a Gaussian profile, providing excellent starting conditions for subsequent manipulation of the polarization.

The next element in the optical pathway is the EOM (360-80, Con-optics), mounted on a V-shaped aluminum block attached to a five-axis alignment mount (9082, New Focus). This scheme allows for manual rotation of the EOM along its longitudinal axis (roll), as well as for fine adjustment of position, pitch, and yaw. Precise control of the orientation is necessary to align the EOM crystal, given its narrow aperture (~ 2 mm) and long length (~ 10 cm). The optical axes of the EOM can be aligned with respect to the incoming polarization by placing a temporary PBS after the EOM, and then oscillating the drive voltage from minimum to maximum range (corresponding to $\alpha = \pm 90^\circ$). As the transmitted intensity is recorded with a photodiode, the EOM housing is rotated until the maximum contrast is observed, signaling polarization changes from linear (vertical) to circular and back to linear (horizontal). While it is possible to rotate the incoming laser polarization instead of rotating the EOM, considerable care must be taken with subsequent polarization alignments.

After the EOM, the beam is expanded to a final waist size of $w \sim 3$ mm and sent to a periscope that elevates the beam height to ~ 20 cm above the

optical table. To minimize depolarization effects arising from nonorthogonal reflections, we use silver mirrors in the periscope, rather than dielectric mirrors. Before the beam enters the microscope, two lenses of equal focal length ($f = 75$ mm) are placed in the optical path, forming a 1:1 telescope, with one of the lenses mounted on a x–y–z translation stage and placed in a plane optically conjugate to the back-focal plane of the objective. This telescope provides a means of steering the trap in the sample plane without beam clipping at the back of the objective (Neuman and Block, 2004; Visscher and Block, 1998). Finally, the beam is coupled into the microscope by reflection from a dichroic mirror, passes through the input $\lambda/4$-waveplate, and reaches the entrance pupil of the objective. We confirmed the EOM-controlled rotation of the laser polarization by removing the microscope objective and monitoring the transmitted intensity after an auxiliary polarization analyzer (a PBS).

The uniformity of the beam polarization is the figure of merit in an OTW, and a few precautions were taken to maintain its quality. First, all mirrors transporting the beam after the EOM into the microscope were aligned at 45° angles with respect to the incoming beam direction to avoid depolarization effects. Second, the fast and slow axes of the EOM were matched to the *S*- and *P*-axes of any subsequent mirror reflections. In this fashion, any phase retardation between the *S* and *P* components is equivalent to an additive constant to the phase retardation generated by the EOM, which can easily be nulled out. Finally, positioning the input $\lambda/4$-waveplate directly below the objective minimizes depolarization effects induced by torque exerted on the mirrors themselves, which would otherwise introduce a spurious torque signature into the output detector.

The apparatus was based on a commercial inverted microscope (Eclipse TE2000-S, Nikon), modified to accommodate the optics needed to couple the trapping beam into the objective and to produce and detect the beam polarization. The vertical arm carrying the microscope condenser was removed and replaced by a structure designed to improve mechanical stability (Fig. 15.4). This structure was formed by two large vertical construction rails (XT95, Thorlabs), cross-linked at the top by a third rail, and further supported by additional beams joining the vertical rails to the optical table. An optical breadboard was suspended vertically from the structure and used to hold the condenser plus all detection optics. We used an oil immersion, high NA objective (100X/1.4NA/PlanApo, part 93110IR, Nikon), which has improved throughput in the near-infrared region and maximizes trapping efficiency while minimizing depolarization effects. The condenser lens (1.4NA, Nikon) was mounted on an x–y–z translation stage, which greatly facilitates alignment. The microscope was set up for bright-field illumination of the sample using a blue LED illumination source (LEDC3, Thorlabs) attached on top of the rail structure. Trapped beads are imaged through the microscope video port using a CCD camera.

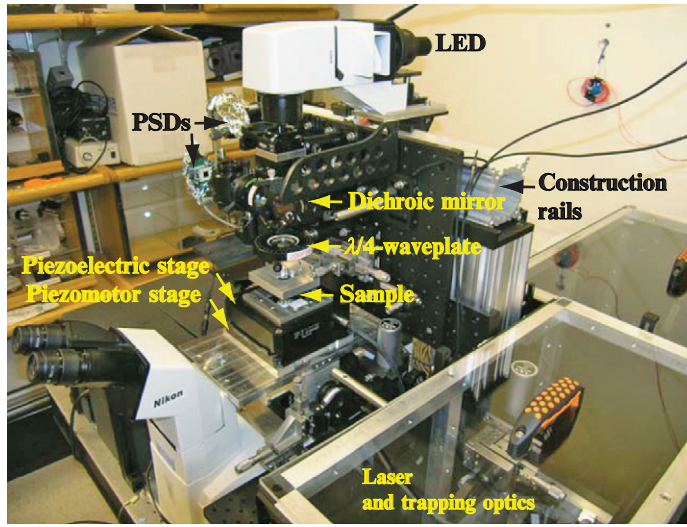

Figure 15.4 Photograph of the OTW instrument, with components as indicated. A commercial Nikon microscope was modified to improve mechanical and optical stability (see main text). The trapping laser, EOM, and associated optics are enclosed in plexiglass boxes (right side) to minimize beam instabilities due to air currents. The sample is held on a 3D piezoelectric stage with a 2D piezomotor substage.

The original Nikon specimen stage was also removed and replaced by a custom-fabricated aluminum mount that supports several items, including the dichroic mirror coupling the laser light into the objective, a precision rotary stage holding the input $\lambda/4$-waveplate below the objective, and piezomotor and piezoelectric stages (M-686.1PM and P-517.3CD, Physik Instrumente). The x–y piezomotor substage is used for coarse positioning of the sample, and features 100-nm step resolution over a 25 mm travel range with enhanced mechanical stability compared to conventional crossed-roller-bearing mechanical stages (Jordan and Anthony, 2009). The x–y–z piezoelectric main stage is used for all fine positioning and has nanometer-level step resolution over $100 \times 100 \times 20$ μm.

3.3. Signal detection and processing

Torque detection from the forward-scattered light exiting the sample chamber is based on an output $\lambda/4$-waveplate placed immediately after the condenser, which maps the right- and left-circular components of the beam polarization into vertical and horizontal linear polarizations, respectively. These polarization components are separated by an analyzer and their intensities measured by separate detectors (Fig. 15.3). In our setup, due to

space constrains, an intermediate dichroic mirror placed after the output $\lambda/4$-waveplate directs the beam toward the analyzer. We use two independent duolateral PSDs with built-in preamplifiers (Pacific Silicon Sensors), aligned for back-focal plane detection (Neuman and Block, 2004) to measure bead displacements and the magnitude of polarization components independently. Each detector produces x, y, and sum (z) voltages for its corresponding circular polarization component, either left or right, to generate V_{lx}, V_{ly}, V_{lz}, V_{rx}, V_{ry}, V_{rz}. The net x, y, z, and torque (τ) signals are obtained by combining these voltages using a simple linear analog electronic circuit, with $x = V_{lx} + V_{rx}$, $y = V_{ly} + V_{ry}$, $z = V_{lz} + V_{rz}$, and $\tau = V_{lz} - V_{rz}$. To generate the z signal, the output beam passes through an aperture that allows the intensity of the central portion of the beam (only) to be measured (Pralle *et al.*, 1999). The position and torque voltages go through low-pass multipole filters to remove noise (3988, Krohn-Hite) and are fed directly into a computer-acquisition board (PCI-6052E, National Instruments), where the signals are further processed by custom software written in LabView (Version 7.1, National Instruments).

4. Fabrication of Anisotropic Particles

4.1. Particles with shape asymmetry

One simple way to obtain oblate particles is to mechanically deform polystyrene microspheres by compression (Oroszi *et al.*, 2006). In our procedure, spherical particles (1.1 μm diameter, Bangs Labs) were suspended in water ($\sim$1–3% by volume) and flattened between a pair of glass microscope slides mounted in a simple vise consisting of two machined aluminum blocks. The vise was padded with 3-mm rubber gaskets to seal the sample and maintain uniform pressure, and compression was obtained by gradually tightening the four ¼-20 bolts holding the vise together, producing an estimated pressure of at least 10^7 Pa. After compression at room temperature for $\sim$2 min, the vice was disassembled and the microspheres were washed off the slide surface. A fraction of these pressure-treated beads ($\sim$1–10%) exhibited an aspect ratio of $\sim$3 when examined by electron microscopy from different angles (Fig. 15.5A shows a top view), and were easily distinguished in the light microscope, where they could be trapped and rotated (Fig. 15.5B). Coating of the surface with chemical or antibody labels is possible either before or after compression. Alternative strategies for deforming uniform polystyrene spheres include compression in conjunction with heat treatment to near the glass point of polystyrene ($\sim$90 °C), or flattening between vise faces in the presence of a mixture of smaller, incompressible silica spheres, which act as spacers to limit the compression distance.

We compressed polystyrene spheres initially coated with either biotin or avidin labels. Using either of these approaches, compressed beads were

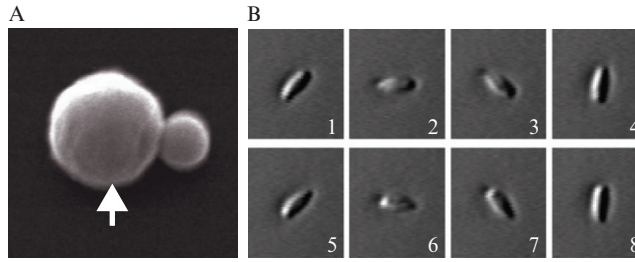

Figure 15.5 Optically anisotropic particles based on form birefringence. (A) Scanning electron microscope picture of an oblate particle (white arrow) created by compressing polystyrene spheres (see main text). The smaller adjacent particle is a 600-nm silica bead. Field of view is 2.5 × 2.5 μm^2. (B) Kymograph showing a sequence of bright-field images corresponding to a trapped, oblate particle being rotated by the OTW. Time between frames, 0.12 s. Field of view is 2 × 2 μm^2.

attached to one end of a single DNA molecule via a biotin–avidin linkage and tethered to a coverslip surface by the opposite end, and torque was exerted on the DNA. While it is possible to perform single-molecule experiments using compressed beads, the uniform labeling of the entire bead surface can make calibration difficult. If the DNA molecule happens to attach to the bead in a nonequatorial position—which, statistically, is the most likely occurrence—the tethered particle will tend to adopt an off-axis orientation, leading to signal crosstalk and thereby to the introduction of uncontrolled forces and torques. This difficulty may be circumvented by carefully selecting for those compressed beads that happen to be tethered by an equatorial point, but these are comparatively rare and may be difficult to identify. However, despite the random variation present in points of attachment, we found compressed beads to be extremely useful during alignment and initial testing phases of the OTW calibration. Because their shape asymmetry is readily seen in the light microscope, it becomes possible to monitor bead rotation using an independent method that does not rely on PSD signals, such as video tracking. This permits measurement of the rotation angle even when the laser trap is off, a helpful trait that we used to confirm the formation of rotationally constrained DNA tethers (see Section 6), by twisting DNA molecules attached to compressed beads and observing unwinding after the trapping beam is blocked.

4.2. Particles with optical asymmetry

Conventional microlithographic techniques can be employed to manufacture birefringent particles of specific shapes in a controlled and reproducible fashion (Deufel *et al.*, 2007). Although chemically produced particles of birefringent materials, such as vaterite, have been used to apply torque in previous applications (Bishop *et al.*, 2004; Funk *et al.*, 2009), lithography

offers several advantages. First, the particles can be chemically derivatized for biological labeling on specific surfaces, facilitating their vertical orientation when tethered in surface-based assays, thereby minimizing undesired forces and torques. Second, micro- or nanofabrication methods can yield large numbers of uniform particles, whose sizes can easily be controlled by changing mask features or adjusting etching parameters. Finally, among the many possible birefringent materials that might be used, in principle, quartz is chemically stable, readily available in wafer form at relatively low cost, and suitable for use with a variety of established etching chemistries, making it a natural choice for OTW applications.

Here, we present a protocol to produce cylinder-shaped particles by a single lithographic exposure of a quartz wafer. The particles are designed to have their extraordinary optical axis perpendicular to the axis of cylindrical symmetry, and are chemically functionalized at only one of the bases (Fig. 15.6). Our protocol was developed from a previous implementation (Deufel *et al.*, 2007), but modified to comply with restrictions imposed by the Stanford Nanofabrication Facility, which precluded placing antireflective coatings on the back sides of wafers.

4.2.1. Mask design and wafers

Reticle design typically depends on the stepper system used. To produce arrays of upright cylinders 400–700 nm in diameter, we divide the mask into 4×4 mm^2 areas, at wafer level, each with about 10^7 evenly spaced octagons of a particular size. Lithographic imaging of tiny octagon (or square) shapes in the mask produces nearly circular patterns on wafers after UV exposure, due to light diffraction effects. The exposure to create uniform patterns of small, high aspect ratio cylinders can reach the practical limit of i-line steppers, especially with a transparent substrate. If multiple patterned regions are placed on a single mask, it is therefore advisable to select just one or two patterns and place them in the center of the reticle, thereby reducing possible astigmatism from the outermost part of the stepper lens. We use 4 in. X-cut, single-crystal quartz wafers with double-side polish (University Wafer).

4.2.2. Protocol

1. Clean the wafer in hot piranha solution (9:1 mixture of H_2SO_4 and H_2O_2, 120 °C) for 20 min. Rinse in water followed by a spin rinse dryer cycle.
2. Functionalize surface for biological labeling with 3-aminopropyltriethoxysilane (APTES) or any other desired organosilane coupling reagent:
   i. Add 0.6 ml of APTES (99%, Sigma-Aldrich) to 30 ml ethanol solution (95% (v/v) ethanol, 5% (v/v) water, pH 5.0 using acetic acid).

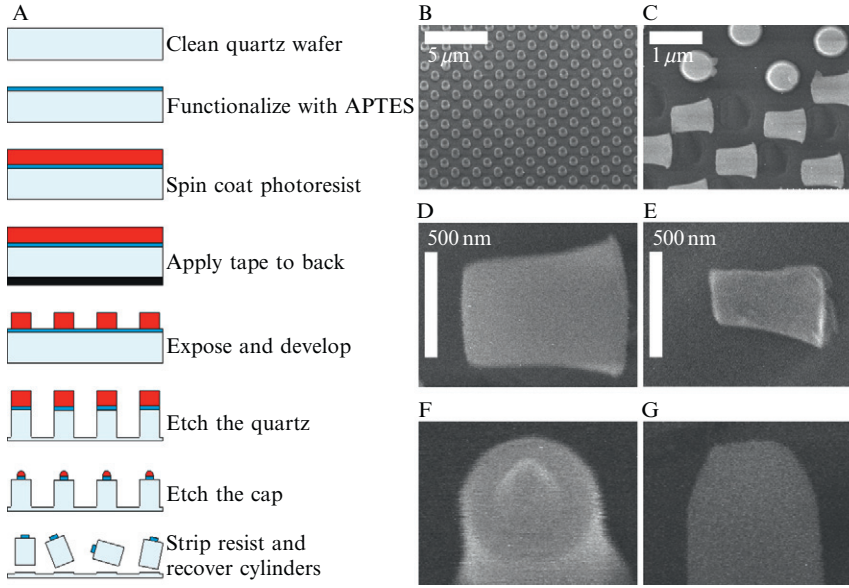

Figure 15.6 Fabrication of birefringent quartz cylinders. (A) Schematic showing the major steps of the fabrication protocol. SEM images of the cylinders during fabrication are shown on the wafer after etching (B) and after cutting (C). (D, E) Examples of particles made with different final sizes. The functionalized area at the top of cylinders may be minimized by shrinking resist (F) or the cylinder itself (G).

ii. Place wafer in solution and sonicate for 5 min.
iii. Rinse by sonicating wafer for 30 s in 50 ml methanol, three times.
iv. Cure in oven for 20 min at 115 °C.

3. Spin coat 1.0 μm photoresist (Megaposit SPR 955-CM, Rohm and Haas Company) onto wafer. We use a Suss MicroTec ACS200 spin coater for these steps:
   i. 1700 rpm, 20 s, followed by edge bead removal (Microposit EC solvent 13) and a final spin at 1200 rpm, 8 s.
   ii. Bake for 90 s on a 90 °C hotplate.
4. Apply dicing tape (Z18551-7.50, Semiconductor Equipment Corporation) to the back side of the wafer and cut along the wafer edge. The use of tape prevents reflections from the stepper exposure chuck and avoids using extra antireflective coatings that may interact with the chuck surface.
5. Expose the pattern. We use an ASML PAS 5500/60 i-line stepper with 5× magnification and a 110 mJ cm^{-2} dose. Adjustments of focus and tilt offsets are necessary for optimal uniformity.
6. Remove tape and bake wafer for 90 s on a 110 °C hot plate.

7. Manually develop the wafer by placing it in the developer (Megaposit MF-26A, Rohm and Haas Company) for 30 s and then gently agitate in solution for an additional 30 s. Rinse in a water beaker and air-blow dry. The manual developing procedure reduces the risk of breaking the high-aspect-ratio resist posts.
8. UV cure for 15 min followed by 1 h bake in 110 °C oven.
9. (Optional) Instead of the previous step, the resist can be cured using a Fusion UV Cure System, which combines high-intensity UV light with a fast temperature ramp (100–200 °C over 45 s). This can improve resist selectivity during the etching process, leading to more vertical cylinder side walls.
10. Etch the wafer. We use an Applied Materials Precision 5000 Etcher at the following settings: power 50 W, pressure 10 mTorr, gas flow 36 sccm CHF_3 and 36 sccm CF_4, magnetic field 30 G, and helium cooling 5 Torr. The resulting etch rate is $\sim$150 Å min^{-1}.
11. (Optional) To reduce the APTES-coated area at the top of the cylinder, an additional dry-etching step can be performed using O_2 plasma for 3 min in a Matrix Plasma Asher (3.75 Torr, 450 W, 100 °C, pins down). As the remaining resist cap is etched, the outer rim of the top quartz surface is exposed to the plasma (Fig. 15.6F), removing the APTES in this region. The linking of biological molecules can thereby be concentrated toward the center of the cylinder, reducing any potential wobbling of the particle during rotation in the optical trap. Another way to reduce the top area is to perform Step 10 until the top cylinder diameter shrinks as a result of a diminished resist layer (Fig. 15.6G).
12. The remaining resist is stripped by rinsing and sonicating in acetone for 20 min.
13. Quartz cylinders are recovered by manually scraping the wafer surface with a microtome blade and collecting the material in a test tube. This can be done in the presence of liquid, such as buffer or cross-linking reagents, to maximize yield.
14. The cylinders are functionalized with coupling proteins of interest, such as avidin, by cross-linking to the primary amines in the APTES using a conventional glutaraldehyde kit (Cat. #: 19540, Polysciences).

In the light microscope, nanofabricated quartz cylinders appear as thick, short rods that can be optically trapped with ease. As expected, trapped cylinders align themselves with their long axis along the direction of beam propagation, with the functionalized surface facing toward (or away from) the coverglass surface—an ideal geometry for producing tethers in a surface-based, single-molecule assay.

5. Instrument Calibration

5.1. Standard optical tweezers calibration methods

A number of well-established methods have been developed to calibrate the stiffness of an optical trap (κ) acting on *spherical* beads. The most common methods are based on analysis of measurements of particle *variance*, *power spectrum*, or *Stokes' drag*, and have been described in greater detail previously (Neuman and Block, 2004; Svoboda and Block, 1994; Visscher and Block, 1998). Briefly, under low Reynolds number conditions, the thermal motions of a trapped bead in solution depend on the bead's viscous drag coefficient and the trap stiffness. The simplest of all calibration methods is variance-based, and uses the positional variance of a bead $\langle x^2 \rangle$ in combination with the "equipartition theorem" to compute the stiffness from $\kappa_x = \langle x^2 \rangle / k_B T$, where $k_B T$ is the thermal energy. In the power spectrum method, the frequency-dependent amplitude of positional fluctuations is computed, and data are fitted with the behavior of a thermal particle bound in a harmonic potential, which is a Lorentzian function. The spectral roll-off frequency of the fit, $f_c = 1/(2\pi t_0)$, where t_0 is the relaxation time of the bead, can be used to obtain the trap stiffness through the relation $\kappa_x = \beta / t_0$, assuming that the drag coefficient of the spherical particle, $\beta = 6\pi\eta a$, is known, where η is the viscosity and a is the radius. Finally, in the Stokes' drag method, the trapped sphere is subjected to a constant fluid velocity, v_x, and its displacement from the equilibrium position is measured. Flow is typically created by moving the piezoelectric stage holding the sample at constant velocity (e.g., using a triangle wave). The dependence of the bead displacement, x, on v_x has slope $t_0 = \beta / \kappa_x$, from which κ_x can be obtained.

All three methods require a prior calibration of the PSD voltage, $V_{x,}$, as a function of x, the true displacement from the equilibrium position. In a configuration where the same laser beam is used both for trapping and position detection, the calibration of $V(x)$ is typically achieved by scanning a bead immobilized on the coverglass surface across the laser beam, taking care to perform the scanning directly through the trap center. In 1D, the PSD response is well fit by the derivative of a Gaussian function (Allersma *et al.*, 1998), and from the linear, central, part of the profile the conversion factor from nanometers to volts, ξ, can be obtained. Alternatively, in 2D, the immobilized bead can be raster-scanned throughout the trapping area, and the resulting voltage profile can be fit with a 2D polynomial (Lang *et al.*, 2002).

Although fairly straightforward to implement, these calibration methods generally require knowledge of the particle drag coefficient, which is influenced by its shape and the proximity of any nearby surfaces (Svoboda and Block, 1994). Alternatively, the power spectrum and Stokes' drag calibration methods can be combined to yield experimental estimates for

ξ, κ, and β for trapped particles of any shape. To do so, first the power spectrum of the V_x signal is computed, from which the roll-off frequency $f_c = 1/(2\pi t_0) = \kappa_x/(2\pi\beta)$ and the amplitude at zero frequency, $\widetilde{P}_x = k_B T/(\kappa_x \pi^2 f_c \xi^2)$, are obtained. Next, the Stokes' drag method is used to find V_x versus fluid velocity, v, yielding a linear relationship with slope $s = \beta/\kappa\xi$. The last three equations are combined to yield $\kappa_x = 4k_B T f_c s^2/\widetilde{P}_x$, $\beta = 2k_B T s^2/\pi\widetilde{P}_x$, and $\xi = 1/(2\pi s f_c)$, as functions of the experimentally measured parameters s (V nm^{-1} s), f_c (s^{-1}), and $\widetilde{P}_x$ (V^2 Hz^{-1}).

5.2. Force calibration

The calibration method just discussed may be applied immediately to the case of trapped, nonspherical particles in the OTW along directions transverse to the beam propagation direction (x, y). Because nonspherical particles do not bind to a surface in a unique orientation, the traditional method of scanning the beam diametrically across a stuck bead to obtain the volts-to-nanometers conversion factor poses problems with oblate ellipsoids or quartz cylinders. Instead, we performed x- and y-calibrations using the combined power spectrum Stokes' drag method of the previous section: sample results for quartz cylinders are shown in Fig. 15.7. The Stokes' drag results display the expected linear relationships between $V_{x,y}$ and $v_{x,y}$, and the power spectra calculated from the x- and y-signals are well fit by Lorentzian functions with the parameters shown in the caption of Fig. 15.7.

Careful calibration of the optical trap in the axial direction is, operationally speaking, the most important of all because the OTW apparatus is mainly intended for the simultaneous application of torque and vertical loads. Calibration in the z-direction, however, involves different considerations compared to x–y (Neuman and Block, 2004). First, the finite axial trapping depth restricts the range over which the Stokes' drag calibration method can be performed. Second, when the sample chamber is moved vertically, an intensity modulation at the detector arises from interference between the forward-scattered light and light reflected from the coverslip/solution interface, an effect that must be taken into account. Finally, motions of the sample chamber relative to the microscope objective will induce a focal shift that displaces the trap axial position (Neuman *et al.*, 2005). Recent efforts aimed at addressing some of these limitations include the unzipping of a known DNA template to obtain a calibrated reference (Deufel and Wang, 2006) or performing back-scattered light detection (optionally, with spatial filtering) to reduce systematic errors (Carter *et al.*, 2007; Sischka *et al.*, 2008).

In our instrument, we performed z-calibrations of force and displacement using quartz cylinders by taking advantage of the stable orientation of these nanofabricated particles within the trap. First, we obtained f_c and $\widetilde{P}_z$ from the power spectrum of the z signal (Fig. 15.7). Next, we impaled a trapped, vertically oriented cylinder on the coverglass by adjusting the

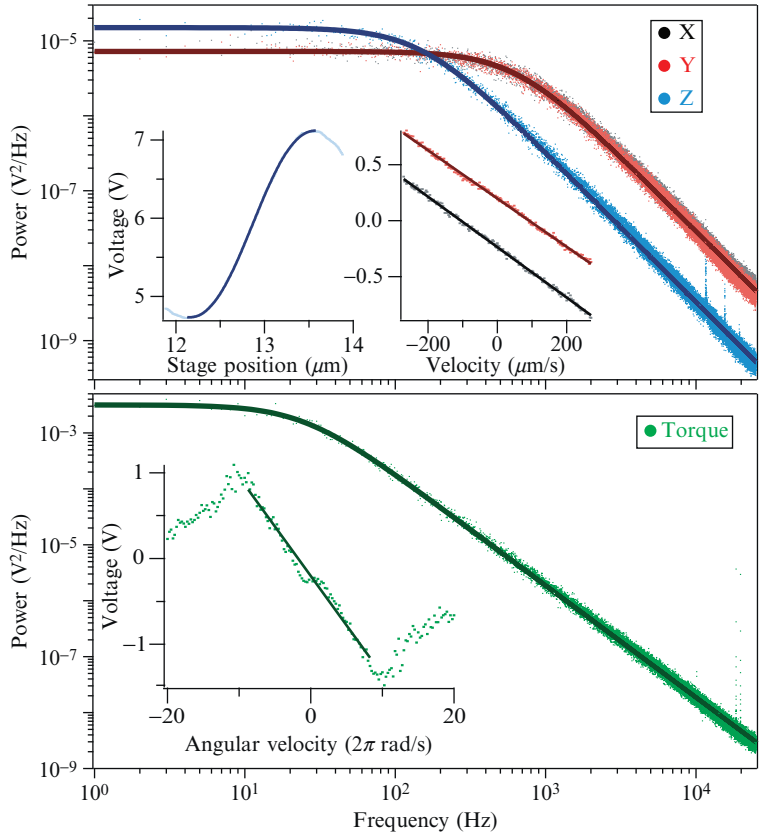

Figure 15.7 Calibration of the optical torque wrench using a quartz cylinder. (Top)-Calibrations of the linear dimensions. First, the power spectra for x, y, and z signals were computed and fit to Lorentzian functions, giving roll-off frequencies $f_{c,x} = 639 \pm 1$ Hz, $f_{c,y} = 631 \pm 1$ Hz, $f_{c,z} = 147.2 \pm 0.2$ Hz, and zero-frequency amplitudes $\widetilde{P}_x = (1.158 \pm 0.003) \times 10^{-6}$ V^2 Hz^{-1}, $\widetilde{P}_y = (1.148 \pm 0.003) \times 10^{-6}$ V^2 Hz^{-1}, and $\widetilde{P}_z = (2.382 \pm 0.005) \times 10^{-6}$ V^2 Hz^{-1}. Next, linefits to Stokes' drag measurements in x and y (Right inset) provided the slopes $s_x = (2.255 \pm 0.008) \times 10^{-6}$ V s nm^{-1} and $s_y = (2.158 \pm 0.008) \times 10^{-6}$ V s nm^{-1}, which were combined with the power spectral results to yield $\xi_x = 1/(2\pi s_x f_{c,x}) = 110\,\text{nm}\,\text{V}^{-1}$ and $\xi_y = 117\,\text{nm}\,\text{V}^{-1}$. For the z signal, vertical scanning of a fixed cylinder (Left inset) produced a record well fit by the derivative of a Gaussian (amplitude $A = (1.395 \pm 0.006) \times 10^3$ V nm, S.D. $\sigma = 708 \pm 2$ nm), from which we obtain $\xi_z = \sigma^2/A = 359\,\text{nm}\,\text{V}^{-1}$. These measurements were combined to obtain the trap stiffnesses $\kappa_x = 4.5 \times 10^{-2}\,\text{pN}\,\text{nm}^{-1}$, $\kappa_y = 4.1 \times 10^{-2}\,\text{pN}\,\text{nm}^{-1}$, and $\kappa_z = 9.1 \times 10^{-3}$ pN nm^{-1}. (Bottom) Calibration of torque. A procedure analogous to the linear x, y cases was carried out. From the experimentally measured values, $f_{c,\tau} = 24.29 \pm 0.05$ Hz, $\widetilde{P}_\tau = (5.04 \pm 0.01) \times 10^{-4}$ V^2 Hz^{-1}, and $s_\tau = (1.84 \pm 0.03) \times 10^{-2}$ V s rad^{-1}, the volts-to-radians conversion factor $\xi_\tau = 1/(2\pi s_\tau f_{c,\tau}) = 0.37\,\text{rad}\,\text{V}^{-1}$ and the angular trap stiffness $\kappa_\tau = 4k_\text{B}Tf_{c,\tau}s_\tau^2/\widetilde{P}_\tau = 264\,\text{pN nm rad}^{-1}$ were obtained. All power spectrum records represent averages from 50 measurements sampled at 66 kHz. For these measurements, the trapping laser power was ~20 mW (measured before entry into the objective rear pupil).

piezoelectric stage position until its base bound nonspecifically to the surface. Vertical scanning of the piezoelectric stage while recording V_z yielded the required voltage–displacement calibration factor, ξ_z (nm V^{-1}). Scanning a surface-bound cylinder axially is effective because the trap stabilizes the vertical orientation, contrary to the x–y case, where transverse scanning tends to tilt the particle. The axial stiffness is calculated as before from $\kappa_z = k_B T/(\widetilde{P}_z \xi^2 \pi^2 f_c)$. Using spherical test beads, we have compared calibrations obtained by "parking" the particle on the surface with previous methods, and obtained good agreement (data not shown).

5.3. Torque calibration

Torque calibration may be carried out using methods that are entirely analogous to those used for spatial displacement (La Porta and Wang, 2004). In the OTW apparatus described here, the input polarization angle is automatically known (relative to some arbitrary reference), and is proportional to the EOM input voltage. A rotational Stokes' drag method can therefore be implemented by periodically adjusting the EOM voltage such that the input polarization changes with a fixed angular velocity (ω_θ). The power spectrum of the torque signal voltage (V_τ) can also be readily computed. We therefore have used a combination of power spectrum and rotational Stokes' drag techniques to obtain the torque signal volts-to-radians conversion factor, ξ_τ, the trap angular stiffness, κ_τ, and the rotational drag coefficient of the trapped particle, β_τ. The experimental quantities measured were the slope of the V_τ versus ω_θ line, along with the roll-off frequency and zero-frequency amplitude of the angular power spectrum.

Figure 15.7 shows results from torque and force calibrations for a quartz cylinder. Fits of the various calibration signals to the expected functional forms are excellent, and the experimental parameters derived from such fits have uncertainties of less than 1%. For small displacements (< 150 nm) and small angles ($< 20°$), the detector signals are linear. As anticipated, modest laser power (10–50 mW) is sufficient to provide tight confinement of particles translationally as well as rotationally, making it possible to exert transverse and axial forces in excess of 20 and 5 pN, respectively, and torques of at least 300 pN nm.

5.4. Implementation of an optical torque clamp

An anisotropic particle trapped in a laser beam with fixed linear polarization will undergo rotational thermal motion whose amplitude depends on the angular trapping stiffness. In this "passive" mode, the mean torque exerted by the trap on the particle is zero, and nonzero torques will develop only if the particle is forced to change its angular orientation, for example, when twisted by a molecular motor. While it is possible to study rotary biomolecular processes in the passive mode, data taken under more precisely defined

conditions, such as under constant applied torque, can provide more specific information. A torque clamp is the rotary analog of a force clamp, which provides high-resolution data on molecular displacements (Visscher and Block, 1998). We implemented a torque clamp mode by creating a servo loop that feeds the torque signal back into an external electronic circuit driving the EOM (Fig. 15.8A). Although it may be possible to implement

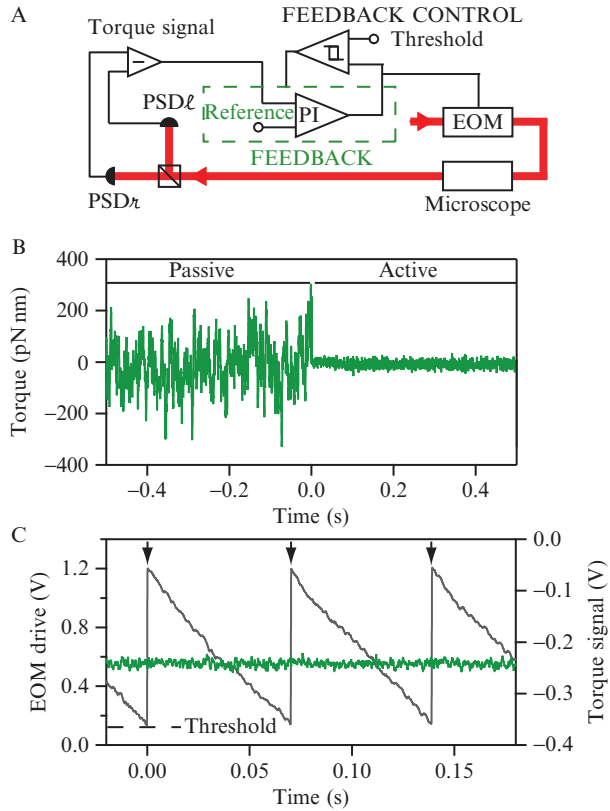

Figure 15.8 Realization of a continuous torque clamp. (A) Schematic showing the signals and feedback loops used in the OTW. Constant torque is maintained by a servo loop that feeds the torque signal into a proportional–integral circuit controlling the EOM. An additional "feedback control" circuit extends the dynamic range of the EOM to maintain constant torque over continuous rotations (see main text). (B) Demonstration of the torque clamp. In passive mode, the torque servo loop is disabled, and the signal reflects the rotational Brownian motion of an oblate trapped particle. At time $t = 0$ s, the servo loop is closed, clamping the torque at $\tau = 0$ pN nm. (C) To clamp torque at nonzero values, the EOM drive signal (gray sawtooth curve) flips by an amount value corresponding to $\pm 180°$ once an angular threshold is reached. These rapid reversals (black arrows) are automatically executed by the feedback control circuit. A nonzero torque signal (green curve) remains constant over unlimited rotations.

feedback control in computer software, we decided instead to employ a dedicated proportional–integral (PI) circuit that circumvents delays associated with computer interrupts. The analog PI controller is based on a single operational amplifier (OP27, Analog Devices) that compares the input torque signal with a reference voltage and sends an output voltage proportional to this difference, stabilized by an integral filter that smoothes the response (Gardner, 2005).

The torque clamp works for particles with either form or material birefringence. In the example shown in Fig. 15.8B, an oblate particle is first trapped in the passive mode and then feedback mode is established, keeping the particle at constant (here, zero) torque. As the active mode is enabled, the rms value of the torque signal (τ_{rms}) decreases by sevenfold compared to the rms amplitude of thermal fluctuations in the passive mode, yielding $\tau_{rms} = 14$ pN nm. The torque clamp has high bandwidth ($\sim$10 kHz) and is limited chiefly by the angular relaxation time of the particle under low Reynolds number conditions.

The restricted dynamic range of an EOM ($\pm 180°$) constrains any simple servo loop in keeping the torque constant over multiple revolutions. To overcome this limitation, we included an additional circuit that monitors the EOM drive signal using a microcontroller (Arduino deicimila, Arduino, Italy). Once an angular threshold is reached, the microcontroller triggers an analog switch (AD7512, Analog Devices) that momentarily disables the feedback, flips the polarization by $\pm 180°$, and reenables the servo loop (Fig. 15.8A). The performance of this circuit is illustrated in Fig. 15.8C, where rapid EOM voltage jumps are evident, but during which the torque signal reflects persistent clamp conditions. Because polarization reversals are completed within 10 μs, the bandwidth of the servo loop is unaffected.

6. Simultaneous Application of Force and Torque Using Optical Tweezers

6.1. Twisting single DNA molecules under tension

The nanomechanical properties of DNA have been extensively studied at the single-molecule level using magnetic tweezers (Lionnet *et al.*, 2008), but only recently using optical traps (Forth *et al.*, 2008). To demonstrate the capabilities of our calibrated instrument, we studied the supercoiling of single DNA molecules under tension. Nanofabricated quartz cylinders were tethered to a coverglass surface by a 2.1 kb segment of dsDNA using standard protocols (Lang *et al.*, 2004). Briefly, a dsDNA template was constructed with an array of six digoxigenin labels (spaced at 10 bp intervals) located at the 5′ end of one strand, and six biotin labels (similarly spaced) at

the 5′ end of the complementary strand. Neutravidin-labeled quartz cylinders and template DNA molecules were incubated together at ~100 f*M* in phosphate buffer for several hours at 4 °C. Next, the DNA–cylinder complexes were diluted in PEM80 buffer (80 m*M* Pipes, pH 6.9, 1 m*M* EGTA, 4 m*M* $MgCl_2$) with 20 mg ml^{-1} BSA, introduced into a sample chamber where antibodies against digoxigenin had previously been adsorbed on the coverglass surface, and allowed to bind for 20 min at room temperature. A final wash with PEM80 removed unbound cylinders, and the sample chamber was then sealed and moved to the instrument for measurements. The use of multiple ligands at each end of the DNA molecule hinders free swiveling about the attachment points, creating a rotationally constrained tether, as illustrated in Fig. 15.9. After a tethered bead was identified in the microscope, judging by the restricted Brownian fluctuations, it was captured using the trap and centered with the piezoelectric stage, such that its point of surface attachment was located directly below the trapped cylinder.

The dsDNA tether was then subjected to vertical tension by lowering the piezoelectric stage until the quartz cylinder was displaced below the trap center by a specified distance, Δz, corresponding to a force $F_z = -\kappa_z \cdot \Delta z$, where κ_z is the axial trap stiffness. Then, the bead was rotated by $\pm 180°$ and the corresponding torque signal was recorded. Negligible torque is expected

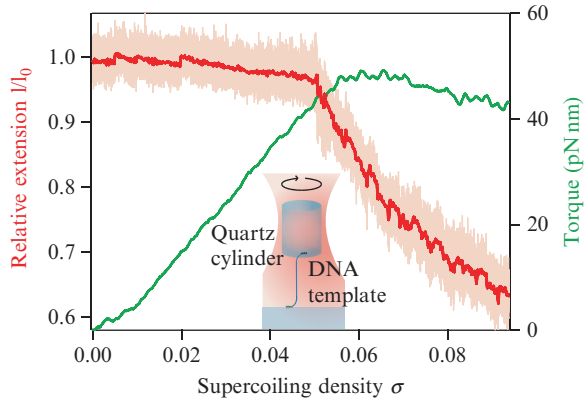

Figure 15.9 Supercoiling of a single 2.1 kbp, dsDNA molecule, tethered to the coverglass surface and a quartz cylinder using multiple dig–antidig and biotin–neutravidin linkages, respectively, to prevent free swiveling at the ends. The DNA molecule was stretched with 3 pN force in the vertical direction while being twisted at a rate of 0.5 turns s^{-1} (inset drawing). The vertical load was kept constant by a software-based PID feedback loop that controlled the piezoelectric stage position with a 20 Hz update rate. The records clearly display the plectonemic transition at $\sigma = 0.05$, and a direct measurement of the imposed torque. Data were collected at 5 kHz (extension, light red trace) and boxcar averaged to 10 Hz (extension, red trace) and 0.5 Hz (torque, green trace).

to develop from the DNA during these initial half-turns at the forces used (2–10 pN). Therefore, any residual signal variations (arising, e.g., from imperfections in the polarization optics) were taken as an average "background" signal that was subtracted from subsequent data (modulo 2π). After acquisition of this background signal, the dsDNA molecule was twisted, typically at rates of 0.5 turn s^{-1} while F_z was clamped by monitoring the PSDs sum voltage and adjusting the piezoelectric stage position as necessary. (Although this vertical force clamp does not take into account variations in the sum signal arising from interference as the coverglass is displaced, we estimate that these effects introduce errors of less than 10% in F_z.) The effect of twisting dsDNA is shown in Fig. 15.9, where the molecular extension and the torque developed are displayed as functions of the degree of supercoiling, $\sigma = n/Lk_0$, where n is the number of turns and Lk_0 is the number of pitch periods spanned by the dsDNA molecule. Initially, the extension remains nearly constant until a torque $\tau \propto n$ develops. After a characteristic number of turns, n_b (corresponding to a torque for bending, τ_b), the energy required for further twisting of the DNA exceeds that for bending, and the molecule begins to buckle, exhibiting a sharp change in length as n_b is reached. As further twisting proceeds, plectonemes are formed in the DNA, and the torque remains roughly constant as the extension of the molecule decreases linearly with n (Strick *et al.*, 1999). Because supercoiling involves close coupling between torque and force exerted on the DNA, the OTW setup is ideal to monitor and control both of these experimental parameters.

7. Conclusions

We have constructed an OTW capable of exerting simultaneous torque and force on micron-sized particles exhibiting either form or material birefringence. Compared to previous implementations, the instrument described here features improved mechanical and optical stability along with a simplified design. We presented procedures for the construction and calibration of the new instrument, along with detailed protocols for fabrication of appropriate birefringent particles. We anticipate that the methods presented here will find applications not only in biophysical studies, but in other fields, including colloid- and nano-engineering.

ACKNOWLEDGMENTS

This work was funded by grant GM57035 from the NIH to S. M. B. Fabrication of quartz microparticles was partially supported by a CIS New User Grant from the Stanford Nanofabrication Facility. We thank Kirsten L. Frieda for providing us with the double-stranded DNA construct used in the supercoiling study.

REFERENCES

Abbondanzieri, E. A., Greenleaf, W. J., Shaevitz, J. W., Landick, R., and Block, S. M. (2005). Direct observation of base-pair stepping by RNA polymerase. *Nature* **438,** 460–465.

Allersma, M. W., Gittes, F., deCastro, M. J., Stewart, R. J., and Schmidt, C. F. (1998). Two-dimensional tracking of ncd motility by back focal plane interferometry. *Biophys. J.* **74,** 1074–1085.

Ashkin, A. (2006). Optical Trapping and Manipulation of Neutral Particles Using Lasers: A Reprint Volume with Commentaries. World Scientific Publishing Company, Singapore.

Ashkin, A., Dziedzic, J. M., Bjorkholm, J. E., and Chu, S. (1986). Observation of a single-beam gradient force optical trap for dielectric particles. *Opt. Lett.* **11,** 288–290.

Berg, H. C. (2003). The rotary motor of bacterial flagella. *Annu. Rev. Biochem.* **72,** 19–54.

Bishop, A. I., Nieminen, T. A., Heckenberg, N. R., and Rubinsztein-Dunlop, H. (2004). Optical microrheology using rotating laser-trapped particles. *Phys. Rev. Lett.* **92,** 198104.

Bryant, Z., Stone, M. D., Gore, J., Smith, S. B., Cozzarelli, N. R., and Bustamante, C. (2003). Structural transitions and elasticity from torque measurements on DNA. *Nature* **424,** 338–341.

Carter, A. R., King, G. M., and Perkins, T. T. (2007). Back-scattered detection provides atomic-scale localization precision, stability, and registration in 3D. *Opt. Express* **15,** 13434–13445.

Deufel, C., and Wang, M. D. (2006). Detection of forces and displacements along the axial direction in an optical trap. *Biophys. J.* **90,** 657–667.

Deufel, C., Forth, S., Simmons, C. R., Dejgosha, S., and Wang, M. D. (2007). Nanofabricated quartz cylinders for angular trapping: DNA supercoiling torque detection. *Nat. Methods* **4,** 223–225.

Dong, K., and Berger, J. M. (2008). Structure and function of DNA topoisomerases. *In* "Protein-Nucleic Acid Interactions: Structural Biology," (P. A. Rice and C. C. Correll, eds.), pp. 234–269. Royal Society of Chemistry, Cambridge.

Forth, S., Deufel, C. Y., Sheinin, M., Daniels, B., Sethna, J. P., and Wang, M. D. (2008). Abrupt buckling transition observed during the plectoneme formation of individual DNA molecules. *Phys. Rev. Lett.* **100,** 148301–148304.

Friese, M. E. J., Rubinsztein-Dunlop, H., Gold, J., Hagberg, P., and Hanstorp, D. (2001). Optically driven micromachine elements. *Appl. Phys. Lett.* **78,** 547–549.

Funk, M., Parkin, S. J., Nieminen, T. A., Heckenberg, N. R., and Rubinsztein-Dunlop, H. (2009). Vaterite twist: Microrheology with AOM controlled optical tweezers. *In* "Proceedings of SPIE. Complex Light and Optical Forces III," (E. J. Galvez, D. L. Andrews, and J. Glückstad, eds.), SPIE, Bellingham, WA, Vol. 7227, p. 72270D.

Gardner, F. M. (2005). Phaselock Techniques. Wiley, Hoboken, NJ.

He, H., Friese, M. E. J., Heckenberg, N. R., and Rubinsztein-Dunlop, H. (1995). Direct observation of transfer of angular momentum to absorptive particles from a laser beam with a phase singularity. *Phys. Rev. Lett.* **75,** 826.

Hua, W., Chung, J., and Gelles, J. (2002). Distinguishing inchworm and hand-over-hand processive kinesin movement by neck rotation measurements. *Science* **295,** 844–848.

Jordan, S. C., and Anthony, P. C. (2009). Design considerations for micro- and nanopositioning: Leveraging the latest for biophysical applications. *Curr. Pharm. Biotechnol.* 10(5), 515–521.

Kar, S., Choi, E. J., Guo, F., Dimitriadis, E. K., Kotova, S. L., and Adhya, S. (2006). Right-handed DNA supercoiling by an octameric form of histone-like protein HU: Modulation of cellular transcription. *J. Biol. Chem.* **281,** 40144–40153.

La Porta, A., and Wang, M. D. (2004). Optical torque wrench: Angular trapping, rotation, and torque detection of quartz microparticles. *Phys. Rev. Lett.* **92,** 190801–190804.

Landau, L. D., Lifshitz, E. M., and Pitaevskii, L. P. (1984). Electrodynamics of Continuous Media. Pergamon Press, Oxford.

Lang, M. J., Asbury, C. L., Shaevitz, J. W., and Block, S. M. (2002). An automated two-dimensional optical force clamp for single molecule studies. *Biophys. J.* **83,** 491–501.

Lang, M. J., Fordyce, P. M., Engh, A. M., Neuman, K. C., and Block, S. M. (2004). Simultaneous, coincident optical trapping and single-molecule fluorescence. *Nat. Methods* **1,** 133.

Lionnet, T., Allemand, J.-F., Revyakin, A., Strick, T. R., Saleh, O. A., Bensimon, D., and Croquette, V. (2008). Single-molecule studies using magnetic traps. *In* ''Single-Molecule Techniques: A Laboratory Manual,'' (P. R. Selvin and T. Ha, eds.), pp. 347–369. Cold Spring Harbor Laboratory Press, Cold Spring Harbor, NY.

Neuman, K. C., and Block, S. M. (2004). Optical trapping. *Rev. Sci. Instrum.* **75,** 2787–2809.

Neuman, K. C., Abbondanzieri, E. A., and Block, S. M. (2005). Measurement of the effective focal shift in an optical trap. *Opt. Lett.* **30,** 1318–1320.

Noji, H., Yasuda, R., Yoshida, M., and Kinosita, K. (1997). Direct observation of the rotation of F1-ATPase. *Nature* **386,** 299–302.

Oroszi, L., Galajda, P., Kirei, H., Bottka, S., and Ormos, P. (2006). Direct measurement of torque in an optical trap and its application to double-strand DNA. *Phys. Rev. Lett.* **97,** 058301–058304.

Pralle, A., Prummer, M., Florin, E. L., Stelzer, E. H. K., and Hörber, J. K. H. (1999). Three-dimensional high-resolution particle tracking for optical tweezers by forward scattered light. *Microsc. Res. Tech.* **44,** 378–386.

Simpson, S. H., and Hanna, S. (2009). Rotation of absorbing spheres in Laguerre–Gaussian beams. *J. Opt. Soc. Am. A* **26,** 173–183.

Sischka, A., Kleimann, C., Hachmann, W., Schafer, M. M., Seuffert, I., Tonsing, K., and Anselmetti, D. (2008). Single beam optical tweezers setup with backscattered light detection for three-dimensional measurements on DNA and nanopores. *Rev. Sci. Instrum.* **79,** 063702.

Smith, S. B., Finzi, L., and Bustamante, C. (1992). Direct mechanical measurements of the elasticity of single DNA molecules by using magnetic beads. *Science* **258,** 1122–1126.

Smith, S. B., Cui, Y., and Bustamante, C. (1996). Overstretching B-DNA: The elastic response of individual double-stranded and single-stranded DNA molecules. *Science* **271,** 795–799.

Strick, T. R., Bensimon, D., and Croquette, V. (1999). Micro-mechanical measurement of the torsional modulus of DNA. *Genetica* **106,** 57–62.

Svoboda, K., and Block, S. M. (1994). Biological applications of optical forces. *Annu. Rev. Biophys. Biom.* **23,** 247–285.

Visscher, K., and Block, S. M. (1998). Versatile optical traps with feedback control. *In* ''Methods in Enzymology,'' (B. V. Richard, ed.), Vol. 298, pp. 460–489. Academic Press, San Diego, CA.

Volpe, G., and Petrov, D. (2006). Torque detection using Brownian fluctuations. *Phys. Rev. Lett.* **97,** 210603.

Wang, M. D., Yin, H., Landick, R., Gelles, J., and Block, S. M. (1997). Stretching DNA with optical tweezers. *Biophys. J.* **72,** 1335–1346.